International Journal of Plasticity 142 (2021) 102996

Contents lists available at ScienceDirect

International Journal of Plasticity

journal homepage: http://www.elsevier.com/locate/ijplas

On the coupling of damage and single crystal plasticity for ductile polycrystalline materials

Bjørn Håkon Frodal [a,*], Susanne Thomesen [a,b], Tore Børvik [a,b], Odd Sture Hopperstad [a,b]

[a] SIMLab – Structural Impact Laboratory, Department of Structural Engineering, NTNU – Norwegian University of Science and Technology, Trondheim, Norway

[b] CASA – Centre for Advanced Structural Analysis, NTNU, Trondheim, Norway

ARTICLE INFO

Keywords:
A. Fracture
B. Crystal plasticity
B. Polycrystalline material
C. Finite elements
Coupled damage

ABSTRACT

A crystal plasticity model accounting for damage evolution and ductile failure in a single crystal due to the presence of voids or micro-cracks is presented. An accurate, robust and computationally efficient single crystal implementation is extended and applied to model the behaviour of different aluminium alloys in the cast and homogenized condition and the extruded condition. A total of four different materials are investigated, in which the yield strength, work hardening, grain structure, crystallographic texture and tensile ductility are unique for each alloy. The coupled damage and single crystal plasticity model is used in three-dimensional polycrystalline finite element analyses of one smooth and two notched axisymmetric tensile specimens for each material. The tensile tests are analysed in Abaqus/Explicit, where each grain is explicitly modelled. An efficient procedure for calibrating the work-hardening parameters for single crystal plasticity models is proposed and used to determine the material parameters from the tension tests of the smooth tensile specimen with high accuracy. The capability of the proposed crystal plasticity model is demonstrated through comparison of finite element simulations and experimental tests. A good agreement is found between the experimental and numerical results, and the various shapes of the failed specimens are well predicted by the crystal plasticity finite element analyses. For one of the extruded aluminium alloys, a diamond-shaped fracture surface is observed in the experiments of the notched tensile specimens and also this unusual shape is captured by the crystal plasticity analyses.

1. Introduction

The process of ductile fracture includes nucleation, growth and coalescence of microscopic voids at second-phase particles or inclusions, and depends markedly on the local stress state and microstructural material characteristics in a complex way (Pineau et al., 2016). Typically, a higher stress level increases the void nucleation rate and a higher stress triaxiality ratio accelerates the void growth. Further, the deviatoric stress state, often characterized by the Lode parameter, influences the propensity for strain localization, in addition to affecting void growth and coalescence (Tekoğlu et al., 2015).

The first studies of ductile failure, employing micromechanical modelling strategies, were those of McClintock (1968) and Rice and

* Corresponding author.
E-mail address: bjorn.h.frodal@ntnu.no (B.H. Frodal).

https://doi.org/10.1016/j.ijplas.2021.102996
Received 12 January 2021; Received in revised form 19 March 2021; Accepted 5 April 2021
Available online 16 April 2021

Tracey (1969), who investigated void growth in an infinite elastic-plastic material containing a single void. McClintock (1968) considered a cylindrical void, whereas Rice and Tracey (1969) investigated the response of a spherical void. Needleman (1972) was the first to use unit cell analyses to study void growth in an elastic-plastic material containing a periodic array of voids. Later, Gurson (1977) used limit analysis considering a spherical void in a von Mises material to derive the yield function for a porous material.

Ductile fracture occurs after significant plastic deformation of the material, and earlier studies have shown that plastic flow and ductile fracture are coupled phenomena. Plastic flow leads to damage evolution by growth and coalescence of voids, i.e., voids will grow in the material due to plastic straining, and coalesce as the inter-void ligaments are subjected to plastic flow localization (Pineau et al., 2016). In addition, strain softening and localization can occur due to damage evolution which again promotes ductile fracture (Tekoğlu et al., 2015). Thus, the plastic properties of a material, such as yield strength, work hardening and plastic anisotropy, can strongly influence its ductility (Frodal et al., 2020a). A higher yield strength tends to increase the void nucleation rate, whereas a higher work-hardening rate can lead to a more dispersed distribution of the plastic flow that could increase the ductility by postponing strain localization. Plastic anisotropy can induce fracture anisotropy, particularly by affecting plastic flow and strain localization (Fourmeau et al., 2011; Frodal et al., 2020a).

The thermo-mechanical processing of metals and alloys influences microstructural characteristics such as the precipitate structure, grain structure and crystallographic texture, and determines the plastic behaviour of these materials (Frodal et al., 2020b). Crystallographic texture is the primary source of plastic anisotropy (Engler and Randle, 2009). Traditionally, plastic anisotropy has been modelled using phenomenological anisotropic plasticity models (e.g., Hill, 1948; Bron and Besson, 2004; Barlat et al., 2005). These models often contain several parameters, which are usually determined from experiments (Fourmeau et al., 2011). In contrast, crystal plasticity theory can be used to determine the plastic flow properties of a material based on information about its crystallographic texture. The grain morphology, the local interactions and inhomogeneities of the mechanical fields of polycrystalline materials can all be explicitly included. In addition, crystal plasticity models are capable of predicting changes in a material's plastic properties by evolving the texture.

Several works have developed porous plasticity models with plastic anisotropy in the matrix material, using phenomenological anisotropic plasticity models (e.g, Benzerga and Besson, 2001; Steglich et al., 2010; Dæhli et al., 2017). A more fundamental way of including plastic anisotropy into the modelling of ductile materials is by using crystal plasticity instead. Single crystal porous plasticity models can be derived using limit analysis or other types of homogenization methods (Han et al., 2013; Paux et al., 2015, 2018; Mbiakop et al., 2015a,b; Ling et al., 2016; Song and Ponte Castañeda, 2017; Joëssel et al., 2018; Siddiq, 2019). The ductile fracture process occurs inside of grains or at the grain boundaries, and the grains could for some materials be one or two orders of magnitude larger than the void-nucleating particles. Consequently, void growth around a particle takes place in a single grain/crystal or possibly within some few grains when the void grows on or in the neighbourhood of the grain boundary. Therefore, it is advantageous to model the matrix behaviour using crystal plasticity instead of phenomenological plasticity models, as the latter only account for the averaged plastic behaviour of a polycrystal. Recently, Savage et al. (2018) compared a novel analytical dilatational model for porous polycrystals and crystal plasticity finite element-based unit cell analyses and found that these simulations showed a more pronounced effect of the third deviatoric stress invariant on yielding than those performed with a phenomenological plasticity model.

The majority of existing studies have developed crystal porous plasticity models and validated them using the unit cell modelling framework. In addition to unit cell simulations, Ling et al. (2016) modelled a notched tensile specimen of single crystals under plane strain tension to assess their crystal porous plasticity model. Khadyko et al. (2021) used their regularized porous crystal plasticity model in two- and three-dimensional finite element simulations of ductile fracture in polycrystalline materials. In contrast, regular crystal plasticity models without ductile failure have been used more frequently in simulations of material samples and small structural components to study other microstructural phenomena (e.g., Wu et al., 2007; Zhang et al., 2007; 2009; Khadyko et al., 2015). One example is the work by Khadyko et al. (2015) who performed crystal plasticity simulations of cylindrical smooth and notched tension specimens for an aluminium alloy. Using crystal plasticity finite element simulations, the unusual rectangular cross-sectional shape observed in the notched experimental tests for the textured aluminium alloy was reproduced.

Single crystal plasticity models can also be combined with different homogenization techniques to describe the behaviour of polycrystalline solids. Such homogenization techniques include: the full-constraint and reduced-constraint Taylor models, different types of self-consistent models, and full-field micromechanical approaches. In this context, Rousselier and Leclercq (2006) included the presence of porous damage in the homogenization procedure by considering an additional self-consistent inclusion representing a void, i.e., an inclusion described by an isotropic porous plasticity model under pure volumetric straining. Further, Rousselier and Luo (2014) proposed a combined void damage and Mohr–Coulomb ductile fracture model in the reduced texture methodology using a self-consistent homogenization technique. They combined the method of Rousselier and Leclercq (2006) with an additional slip rate for each slip system in the reduced texture methodology, which was activated according to the Mohr–Coulomb model at large strains. More recently, Rousselier (2021) proposed a porous plasticity multiscale modelling framework. In this framework, a conventional porous plasticity model is used where the work-hardening response of the matrix flow stress is determined by crystal plasticity combined with the self-consistent homogenization technique and the reduced texture methodology.

Numerical simulations of materials using crystal plasticity models are computationally expensive and such models are rarely used in finite element analyses of structural components. Introducing porous plasticity or damage evolution and ductile failure into the crystal plasticity framework adds another layer of complexity. Due to this additional computational cost, few studies exist where the crystal porous plasticity models available today have been used to study ductile fracture phenomena in polycrystalline solids. Albeit recent developments of spectral crystal plasticity methods using Fast Fourier transforms (denoted CP-FFT) running on high-performance platforms (Eghtesad et al., 2020) allow for full-field micromechanical modelling of high-resolution microstructures, crystal plasticity analyses are still computationally demanding. CP-FFT is rather computational efficient in solving the mechanical

problem, but is limited to periodic boundary conditions. In contrast, the finite element method requires more computational resources, but can be used to solve the mechanical response of a polycrystalline material with any geometry and boundary conditions (Frodal et al., 2019).

In this paper, an accurate, robust and computationally efficient single crystal plasticity model with damage evolution and failure is proposed. This coupled damage and single crystal plasticity model is used in polycrystalline finite element simulations of smooth and notched tensile specimens where each grain is explicitly modelled. To the authors best knowledge, this is the first time engineering material test specimens of polycrystalline materials are analysed using crystal plasticity simulations including damage evolution and ductile fracture. A total of four different materials are considered, where each alloy display different yield strength, work hardening, grain structure, crystallographic texture and tensile ductility, and represent a majority of wrought aluminium alloys. The results from these crystal plasticity finite element analyses are compared to the experimental tests of the different aluminium alloys presented in Thomesen (2019) and Thomesen et al. (2020, 2021), and a good agreement is found between the numerical and experimental results. For all of the aluminium alloys, the various shapes of the failed specimens are well predicted by the crystal plasticity finite element analyses, including the textured alloy that develops anomalous rectangular and diamond-shaped fracture surfaces. The proposed model's ability to describe the behaviour of the distinctly different materials demonstrates its potential in finite element analyses of ductile polycrystalline materials.

2. Materials

In this work, the two aluminium alloys AA6063 and AA6110 are considered. Each alloy is studied in the cast and homogenized state, and in the extruded state. The four materials were all solution heat-treated and artificially aged to peak strength (temper T6) before mechanical testing.

The cast and homogenized materials have equi-axed grain structures with an averaged grain size of 63 μm and 67 μm for the AA6063 and AA6110 alloys, respectively. For the extruded materials, the AA6063 alloy has a recrystallized grain structure comprising almost equi-axed grains measuring 39 μm along the extrusion direction (ED), 36 μm along the transverse direction (TD) and 30 μm along the thickness direction (ND) of the extruded profile. A typical fibrous, non-recrystallized grain structure is found for the extruded AA6110 alloy, where the grains are severely elongated along ED and has a thickness of approximately 4 μm along ND. In addition, the fibrous grain structure comprises smaller sub-grains. The measured area fraction of constituent particles for the materials is approximately 0.006 and 0.008 for the AA6063 and AA6110 alloys, respectively.

Due to the extrusion process, the extruded materials exhibit crystallographic texture, see Fig. 1. The extruded AA6063 alloy has a typical recrystallization texture containing a strong cube texture with a minor Goss component. In contrast, the fibrous AA6110 alloy has a classical deformation texture consisting of a cube texture and orientations along the β-fiber.

For further information about the materials, material characterization and the mechanical testing, the reader is referred to Thomesen (2019) and Thomesen et al. (2020, 2021).

3. Constitutive model

3.1. Crystal plasticity

In this work, a rate-dependent single crystal plasticity formulation is adopted where the plastic deformation is assumed to occur by

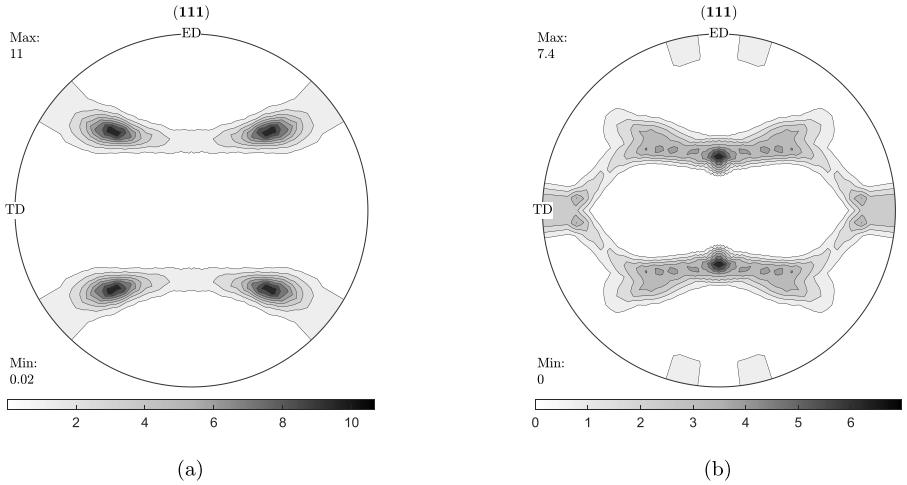

Fig. 1. Pole figures (111) of the initial texture of: (a) the extruded AA6063 alloy, and (b) the extruded AA6110 alloy.

plastic slip on certain crystallographic slip systems, determined by the crystal structure. It is further assumed that the elastic deformations are infinitesimal, while the plastic deformations and rotations may be finite. Here, the single crystal plasticity model presented by Frodal et al. (2019) is extended to include damage evolution and ductile failure.

The velocity gradient $\mathbf{L}$ is additively decomposed into a symmetric and a skew-symmetric part

$$L_{ij} = D_{ij} + W_{ij} \tag{1}$$

where $\mathbf{D}$ is the symmetric rate of deformation tensor and $\mathbf{W}$ is the skew-symmetric spin tensor. These tensors are additively decomposed into elastic and plastic parts

$$D_{ij} = D^e_{ij} + D^p_{ij}, \qquad W_{ij} = W^e_{ij} + W^p_{ij} \tag{2}$$

where $\mathbf{D}^e$ and $\mathbf{D}^p$ are the elastic and plastic rate-of-deformation tensors, respectively. The elastic spin tensor $\mathbf{W}^e$ consists of an infinitesimal elastic contribution and rigid spin of the crystal lattice, whereas $\mathbf{W}^p$ is the plastic spin tensor caused by plastic slip. Plastic slip occurs on certain crystallographic slip systems, thus the plastic parts of the rate of deformation and spin tensors are given by

$$D^p_{ij} = \frac{1}{2}\sum_{\alpha=1}^{N} \dot{\gamma}^{(\alpha)} \left(S^{(\alpha)}_{ij} + S^{(\alpha)}_{ji} \right) \tag{3}$$

$$W^p_{ij} = \frac{1}{2}\sum_{\alpha=1}^{N} \dot{\gamma}^{(\alpha)} \left(S^{(\alpha)}_{ij} - S^{(\alpha)}_{ji} \right) \tag{4}$$

where N is the number of slip systems and $\dot{\gamma}^{(\alpha)}$ is the plastic slip rate on slip system α. For a face-centred cubic (FCC) crystal, $N = 12$. Further, $\mathbf{S}^{(\alpha)} = \mathbf{m}^{(\alpha)} \otimes \mathbf{n}^{(\alpha)}$ is the Schmid tensor, where $\mathbf{m}^{(\alpha)}$ and $\mathbf{n}^{(\alpha)}$ are unit vectors defining the slip direction and slip plane normal, respectively.

Let $\mathbf{e}_i$, $i = 1, 2, 3$, denote the basis for the global coordinate system, and $\widehat{\mathbf{e}}_i$ the basis for a co-rotated coordinate system that rotates with the crystal lattice. The rotation of the lattice is given by the orthogonal rotation tensor R that evolves according to the differential equations

$$\dot{\mathfrak{R}}_{ij} = W^e_{ik}\mathfrak{R}_{kj} \tag{5}$$

which implies that $\widehat{\mathbf{e}}_i = R \cdot \mathbf{e}_i$. The unit vectors $\mathbf{m}^{(\alpha)}$ and $\mathbf{n}^{(\alpha)}$ are not affected by the crystallographic slip and are given by

$$m^{(\alpha)}_i = \mathfrak{R}_{ij}\widehat{m}^{(\alpha)}_j, \quad n^{(\alpha)}_i = \mathfrak{R}_{ij}\widehat{n}^{(\alpha)}_j \tag{6}$$

where the vector components $\widehat{m}^{(\alpha)}_i$ and $\widehat{n}^{(\alpha)}_i$ in the co-rotational coordinate system are constant and defined by the crystal structure.

We will introduce damage within the crystal plasticity framework by introducing an effective stress tensor $\widetilde{\boldsymbol{\sigma}}$ (Lemaitre, 1985), which accounts for the presence of voids or micro-cracks in the single crystal. The effective stress tensor acts on the undamaged portion of the material volume and is defined as

$$\widetilde{\sigma}_{ij} = \frac{\sigma_{ij}}{1-\omega} \tag{7}$$

where $\boldsymbol{\sigma}$ is the Cauchy stress tensor and the damage variable $0 \leq \omega \leq \omega_c < 1$ is zero for a completely undamaged material and reaches the critical value ω_c when failure occurs. In the co-rotated coordinate system, the rate form of the generalized Hooke's law can now be expressed as

$$\dot{\widehat{\widetilde{\sigma}}}_{ij} = \widehat{\mathbb{C}}_{ijkl}\widehat{D}^e_{kl} \tag{8}$$

where the fourth-order elasticity tensor $\mathbb{C}$ of the undamaged portion of the material is assumed invariant of plastic deformation and constant in the co-rotational lattice frame. The Cauchy stress tensor is found after the stress update by means of Equation (7). The elasticity tensor accounts for the elastic anisotropy of the crystal and is defined by the three independent elastic constants $\widehat{c}_{11}$, $\widehat{c}_{12}$ and $\widehat{c}_{44}$. In this case, Equation (8) can be written on matrix form as

$$\begin{bmatrix} \dot{\widehat{\widetilde{\sigma}}}_{11} \\ \dot{\widehat{\widetilde{\sigma}}}_{22} \\ \dot{\widehat{\widetilde{\sigma}}}_{33} \\ \dot{\widehat{\widetilde{\sigma}}}_{12} \\ \dot{\widehat{\widetilde{\sigma}}}_{23} \\ \dot{\widehat{\widetilde{\sigma}}}_{31} \end{bmatrix} = \begin{bmatrix} \widehat{c}_{11} & \widehat{c}_{12} & \widehat{c}_{12} & 0 & 0 & 0 \\ \widehat{c}_{12} & \widehat{c}_{11} & \widehat{c}_{12} & 0 & 0 & 0 \\ \widehat{c}_{12} & \widehat{c}_{12} & \widehat{c}_{11} & 0 & 0 & 0 \\ 0 & 0 & 0 & \widehat{c}_{44} & 0 & 0 \\ 0 & 0 & 0 & 0 & \widehat{c}_{44} & 0 \\ 0 & 0 & 0 & 0 & 0 & \widehat{c}_{44} \end{bmatrix} \begin{bmatrix} \widehat{D}^e_{11} \\ \widehat{D}^e_{22} \\ \widehat{D}^e_{33} \\ 2\widehat{D}^e_{12} \\ 2\widehat{D}^e_{23} \\ 2\widehat{D}^e_{31} \end{bmatrix} \tag{9}$$

The plastic power per unit volume is defined as

$$\mathfrak{D}_p = \sigma_{ij} D^p_{ij} = \sum_{\alpha=1}^{N} \tau^{(\alpha)} \dot{\gamma}^{(\alpha)} = (1-\omega)\widetilde{\sigma}_{ij} D^p_{ij} = (1-\omega) \sum_{\alpha=1}^{N} \widetilde{\tau}^{(\alpha)} \dot{\gamma}^{(\alpha)} \tag{10}$$

where the resolved shear stress $\tau^{(\alpha)}$ acting on slip system α is defined as power conjugate to the plastic slip rate $\dot{\gamma}^{(\alpha)}$. The resolved shear stresses are defined by

$$\tau^{(\alpha)} = \sigma_{ij} S^{(\alpha)}_{ij} = \widehat{\sigma}_{ij} \widehat{S}^{(\alpha)}_{ij} \tag{11}$$

Similarly to Equation (7), the effective resolved shear stress $\widetilde{\tau}^{(\alpha)}$ acting on slip system α in the undamaged portion of the material is defined as

$$\widetilde{\tau}^{(\alpha)} = \widetilde{\sigma}_{ij} S^{(\alpha)}_{ij} = \frac{\sigma_{ij} S^{(\alpha)}_{ij}}{1-\omega} = \frac{\tau^{(\alpha)}}{1-\omega} \tag{12}$$

In this work, the plastic flow is described by the following rate-dependent constitutive relation (Hutchinson, 1976), substituting the resolved shear stresses $\tau^{(\alpha)}$ in the original model with the effective resolved shear stresses $\widetilde{\tau}^{(\alpha)}$, viz.

$$\dot{\gamma}^{(\alpha)} = \dot{\gamma}_0 \left| \frac{\widetilde{\tau}^{(\alpha)}}{\tau^{(\alpha)}_c} \right|^{\frac{1}{m}} \mathrm{sgn}(\widetilde{\tau}^{(\alpha)}) = \dot{\gamma}_0 \left| \frac{\tau^{(\alpha)}}{(1-\omega)\tau^{(\alpha)}_c} \right|^{\frac{1}{m}} \mathrm{sgn}(\tau^{(\alpha)}) \tag{13}$$

where $\dot{\gamma}_0$ is the reference shearing rate, m is the instantaneous strain rate sensitivity, and $\tau^{(\alpha)}_c$ is the critical resolved shear stress on slip system α. The critical resolved shear stresses, with initial value τ_0, evolve according to

$$\dot{\tau}^{(\alpha)}_c = \sum_{\beta=1}^{N} h_{\alpha\beta} |\dot{\gamma}^{(\beta)}| \tag{14}$$

where $h_{\alpha\beta}$ is the instantaneous strain hardening matrix. In this study, we will for simplicity use a matrix on the form $h_{\alpha\beta} = \theta(\Gamma) q_{\alpha\beta}$, where $q_{\alpha\beta}$ is the latent hardening matrix, and $\theta(\Gamma)$ is the work-hardening rate; a function of the accumulated plastic shear strain, Γ, defined as

$$\Gamma = \int_0^t \sum_{\alpha=1}^{N} |\dot{\gamma}^{(\alpha)}| dt \tag{15}$$

The work-hardening rate is given by

$$\theta(\Gamma) = \sum_{k=1}^{N_\tau} \theta_k \exp\left(-\frac{\theta_k}{\tau_k} \Gamma \right) \tag{16}$$

where N_τ is the number of hardening terms, and θ_k and τ_k are the initial hardening rate and saturated value of hardening term k, respectively. In the following, $N_\tau = 2$ will be used.

The damage variable, with initial value ω_0, will here be taken to evolve analogously to the Rice-Tracey model (Rice and Tracey, 1969; Gurson, 1977; Tvergaard, 1981; Rousselier, 1987), viz.

$$\dot{\omega} = \frac{3}{4} q_1 q_2 \omega (1-\omega) \sinh\left(\frac{3}{2} q_2 T \right) \dot{\Gamma} \tag{17}$$

where q_1 and q_2 are material parameters, $\dot{\Gamma}$ is the accumulated plastic shear strain rate, and T is the stress triaxiality ratio defined as

$$T = \frac{\sigma_h}{\sigma_{vm}} \tag{18}$$

where $\sigma_h = \frac{1}{3}\sigma_{kk}$ is the hydrostatic stress, $\sigma_{vm} = \sqrt{\frac{3}{2}\sigma'_{ij}\sigma'_{ij}}$ is the von Mises equivalent stress, and $\boldsymbol{\sigma}'$ is the deviatoric part of the Cauchy stress tensor. Note that the damage evolution rule (Equation (17)) is approximately equal to the Rice-Tracey model for moderate and high stress triaxiality ratios (Rice and Tracey, 1969; Rousselier, 1987) since $\sinh(x) \to \frac{1}{2}\exp(x)$ as $x \to \infty$, and that the evolution of the void volume fraction for the Gurson-Tvergaard model (Gurson, 1977; Tvergaard, 1981) reduces to Equation (17) for small void volume fractions. Here it has been assumed that the accumulated plastic shear strain rate $\dot{\Gamma}$ is two times the equivalent plastic strain rate, see Section 4.2. The chosen damage evolution rule conforms well with experimental findings of void growth in single crystals (Weck et al., 2008; Maire et al., 2011).

The damage evolution rule (Equation (17)) in its current form allows for self-healing if the stress triaxiality ratio is less than zero. This is acceptable if the damage process is governed by void growth, as is the case for traditional porous plasticity or single crystal porous plasticity models, whereas for conventional damage mechanics models this is generally not allowed. Self-healing will not

influence the results presented in this paper, as we study smooth and notched specimens under tension loading only. For other loading scenarios, we propose three valid approaches for extending the damage evolution rule to compressive loading, where the approach applicable for a certain analysis will be dependent on the material.

① The ductile damage is governed by growth of initial voids, and self-healing is allowed as voids may reduce in size under compressive loading.
② The damage originates from voids nucleated around particles, thus self-healing is allowed but the damage variable is not allowed to be reduced below its initial value ω_0.
③ The damage is governed by the presence of, e.g., micro-cracks that only accumulate damage, thus the damage parameter is only allowed to grow as in conventional damage mechanics theory.

The tensile ductility after compression-tension loading has previously been found to depend on the material (Frodal et al., 2019). For materials that exhibit increased tensile ductility after compression loading, ① or ② may be best suited to model the underlying physical mechanisms, while in situations where the tensile ductility is constant or decreased after compression loading, ③ is probably more appropriate.

4. Finite element modelling

4.1. Crystal plasticity finite element models

In this section, we will use the coupled damage and single crystal plasticity model presented above to simulate tension tests of smooth and notched tensile specimens of the aluminium alloys described in Section 2. To this end, we will perform finite element analyses of the polycrystalline materials with random or strong crystallographic textures, using the constitutive model that has been implemented into a user material subroutine (VUMAT) for Abaqus/Explicit (Abaqus, 2019). An explicit integration scheme is utilised for time integration of the rate constitutive equations of single crystal plasticity (Zhang et al., 2014), along with explicit integration of the momentum equations.

Fig. 2 and Fig. 3 display the geometry and finite element mesh of the smooth and notched tensile specimens. Note that different geometries are used for the cast and homogenized alloys than for the extruded alloys due to the limiting dimensions of the extruded profiles (Thomesen, 2019). For the cast and homogenized alloys, the notched specimens (Fig. 2) had an actual diameter between the notch and the threaded ends of 9.47 mm instead of the nominal value of 10 mm after machining. This deviation has previously been investigated and discussed elsewhere, and the reader is referred to Thomesen (2019) and Thomesen et al. (2020) for details. The actual diameter of 9.47 mm is used in the following.

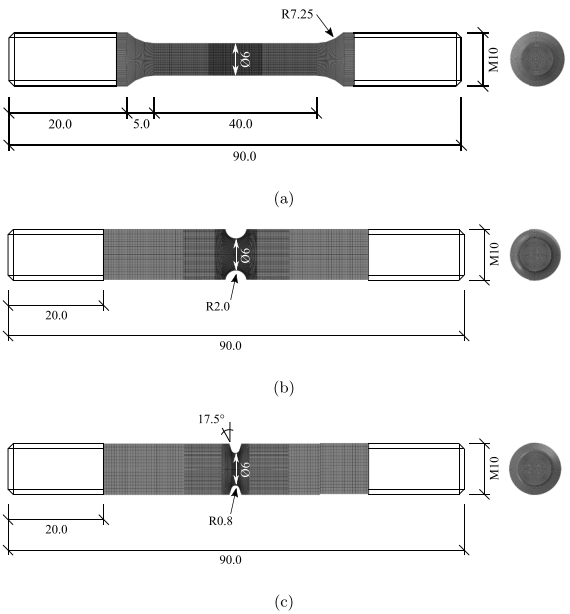

Fig. 2. Tensile specimens used for the cast and homogenized alloys with the finite element mesh imposed: (a) smooth tensile specimen, (b) notched tensile specimen with notch radius 2.0 mm (R2), and (c) notched tensile specimen with notch radius 0.8 mm (R0.8). Dimensions are in mm.

In this work, the tensile axis of the different specimens will be oriented and pulled along TD for the extruded alloys. Due to the orthotropic sample symmetry, only one-eighth of the specimens is modelled to reduce the computational time. Linear eight-node elements with selective reduced integration (C3D8) are used, where the dimension of the centre-most elements is $60 \times 60 \times 60$ μm^3 for the cast and homogenized materials (Fig. 2), and $30 \times 30 \times 30$ μm^3 for the extruded materials (Fig. 3). These element sizes are comparable to the grain size of the materials except for the extruded AA6110 alloy which has a fibrous grain structure, see Section 2. In the following, each grain is represented by a single element. Extensive testing with different finite element meshes showed that the macroscopic response is largely unaffected by variations in the element size, as long as the element size is kept relatively small, i.e., in the same order of magnitude as the grain size. The reader is referred to the recent study of Feather et al. (2021) for further information regarding mesh resolution and element types for crystal plasticity finite element analyses.

All elements/grains in the models are given initial orientations to account for the crystallographic texture of the materials. The crystal orientations are generated using the open source Matlab toolbox MTEX (Bachmann et al., 2010). For the cast and homogenized materials, the orientations are drawn from a "uniformODF" to generate a random texture for these materials, while for the extruded materials the measured texture, i.e., the orientation distribution function (ODF) is used to generate a set of orientations representing the texture for each alloy. In this way, it is ensured that the crystallographic texture of the finite element model of a specimen is as close as possible to the measured texture of the actual material. Fig. 4 displays the finite element mesh of the smooth tensile specimen for the extruded AA6063 alloy depicting the distribution of the crystallographic orientations in the model. Note that the grain boundaries in this study are represented by element boundaries, which is a rather crude approximation of the complex interfaces between grains. With today's limitations in computing power this is a simplification needed for three-dimensional modelling of engineering specimens, but with the presumed evolution of computing architecture a more realistic representation of both the grain structure and boundaries will be achievable in the future, which is already available in representative volume element simulations (Knezevic et al., 2014). The precipitate free zones along the grain boundaries being only a few tens of nanometres wide (Frodal et al., 2020b) are also impossible to include.

The specimens are loaded with a nominal strain rate of $\dot{\epsilon} = 5 \cdot 10^{-4}$ s^{-1} in all simulations, and mass scaling is used to reduce the computational time. Throughout the simulations it is ensured that the response is quasi-static, and it is confirmed that the kinetic energy is negligible.

4.2. Calibration of material parameters

Table 1 contains the crystal plasticity parameters controlling the elastic behaviour, the rate dependence and the self- and latent

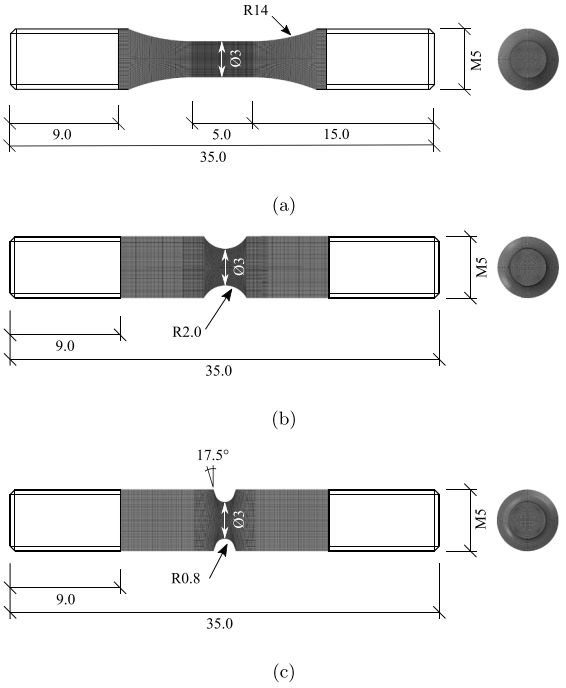

Fig. 3. Tensile specimens used for the extruded alloys with the finite element mesh imposed: (a) smooth tensile specimen, (b) notched tensile specimen with notch radius 2.0 mm (R2), and (c) notched tensile specimen with notch radius 0.8 mm (R0.8). Dimensions are in mm.

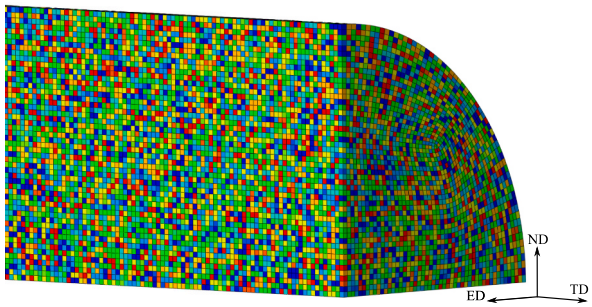

Fig. 4. Finite element mesh of the smooth tensile specimen's centre for the extruded AA6063 alloy with distributed crystallographic grain orientations, where each element corresponds to a grain. The value of the third Euler angle ϕ_2 is represented by different colors. (For interpretation of the references to color in this figure legend, the reader is referred to the Web version of this article.)

hardening, which are common for a broad range of aluminium alloys found in the literature. These parameters are assumed constant for the materials at hand, while the parameters governing initial slip resistance, work hardening, damage and failure are dependent upon the material processing and alloy composition. The chosen self- and latent hardening parameters have previously been shown to conform well with experimental results of aluminium alloys (Khadyko et al., 2016; Zecevic and Knezevic, 2018).

Since the numerical simulations of the specimens are quite computationally expensive, an efficient and accurate method for calibrating the material parameters is needed. We will first propose a method for calibrating the initial slip resistance and work-hardening parameters by simulating the smooth tensile specimens. From the experimental tests (Thomesen, 2019; Thomesen et al., 2020, 2021) and the following finite element simulations, the force F and diameters D_1 and D_3 of the minimum cross-section in two perpendicular material directions were continuously measured to fracture. For the extruded alloys, D_1 and D_3 are the diameters along ED and ND, respectively. From these measurements, the true stress and logarithmic strain, both averaged over the minimum cross-section area, are calculated as

$$\sigma_t = \frac{F}{A}, \quad \epsilon_l = \ln\left(\frac{A_0}{A}\right) \tag{19}$$

where A_0 is the initial cross-section area of the specimen, and plastic incompressibility and negligible elastic strains are assumed. The minimum cross-section area of the test specimen is given by

$$A = \frac{\pi}{4} D_1 D_3 \tag{20}$$

To ease the calibration of the work-hardening parameters, and to compensate for the hydrostatic stress introduced by diffuse necking, the Bridgman corrected stress is calculated as

$$\overline{\sigma} = \begin{cases} \sigma_t & \epsilon^p \leq \epsilon_u^p \\ \dfrac{\sigma_t}{\left(1 + 2\dfrac{R}{a}\right)\ln\left(1 + \dfrac{a}{2R}\right)} & \epsilon^p > \epsilon_u^p \end{cases} \tag{21}$$

where ϵ^p is the logarithmic plastic strain, and ϵ_u^p is the plastic strain at necking. The ratio of the equivalent specimen radius a and the curvature radius R of the neck is estimated by the empirical expression of Le Roy et al. (1981) as

$$\frac{a}{R} = 1.11\left(\epsilon^p - \epsilon_u^p\right), \quad \epsilon^p > \epsilon_u^p \tag{22}$$

In the optimization procedure, the difference in the Bridgman corrected stress versus plastic strain curve between the experiments and the numerical simulations is minimized to obtain the initial slip resistance and work-hardening parameters as follows:

1. The target $\overline{\sigma}_{exp}(\epsilon^p)$ curve, i.e., the experimental Bridgman corrected stress versus plastic strain curve up to failure, is calculated based on the experimental data using Equations 19–22.

Table 1
Crystal plasticity parameters governing elasticity, rate sensitivity and latent hardening (Frodal et al., 2019).

$\widehat{c}_{11}$ (MPa)	$\widehat{c}_{12}$ (MPa)	$\widehat{c}_{44}$ (MPa)	$\dot{\gamma}_0$ (s^{-1})	m	$q_{\alpha\beta}$
106 430	60 350	28 210	0.010	0.005	1.0 if $\alpha = \beta$ 1.4 if $\alpha \neq \beta$

2. An initial guess for the initial slip resistance τ_0^0 and the work-hardening parameters $\theta_1^0, \tau_1^0, \theta_2^0, \tau_2^0$ is made by assuming a constant Taylor factor M and performing step 8.
3. A finite element analysis of the smooth tensile specimen is performed with the parameters $\tau_0^n, \theta_1^n, \tau_1^n, \theta_2^n, \tau_2^n$ for iteration n.
4. The numerical $\overline{\sigma}(\epsilon^p)$ curve is calculated from the FE simulation using Equations 19–22.
5. We assume here that the accumulated plastic shear strain Γ over the minimum cross-section area is proportional to the plastic strain ϵ^p, viz. $\Gamma = \kappa\epsilon^p$, where κ is found to be approximately 2.
6. By integration of Equation (16) with the above assumption, we get

$$\tau_{cr}(\epsilon^p) = \tau_0 + \sum_{i=1}^{2} \tau_i \left(1 - \exp\left(-\frac{\theta_i}{\tau_i}\kappa\epsilon^p\right)\right) \tag{23}$$

7. Based on the parameters $\tau_0^n, \theta_1^n, \tau_1^n, \theta_2^n, \tau_2^n$, we calculate an approximate Taylor factor for the material as $M_n(\epsilon^p) = \frac{\overline{\sigma}_n(\epsilon^p)}{\tau_{cr,n}(\epsilon^p)}$ for iteration n.
8. This Taylor factor is used to calibrate a new set of parameters $\tau_0^{n+1}, \theta_1^{n+1}, \tau_1^{n+1}, \theta_2^{n+1}, \tau_2^{n+1}$ by performing a non-linear optimization of $\overline{\sigma}(\epsilon^p) = M_n(\epsilon^p)\tau_{cr,n+1}(\epsilon^p)$ to the target curve $\overline{\sigma}_{exp}(\epsilon^p)$.
9. The iteration counter is incremented and steps 3–8 are repeated until the resulting numerical curve is accepted.

In general, after 2–3 iterations the parameters are accepted and the mean squared error between the experimental and numerical true stress versus logarithmic strain curve is less than 10^{-5}. Note that the Bridgman corrected stress (Equation (21)) is only valid for isotropic materials. However, the calibration procedure described above is also valid for anisotropic materials. The Bridgman stress correction is only performed to get a better estimate of the Taylor factor for each material and does not influence the final calibrated slip resistance parameters. Note also that Equations 21–23 are only used in the calibration procedure to find the slip resistance parameters, and these equations will not be used any further in the following. Table 2 contains the optimized slip resistance parameters for the cast and homogenized (Cast & H.) and the extruded materials valid to fracture.

Fig. 5 displays the approximate Taylor factor versus plastic strain curves calculated from the final finite element analyses of the smooth tensile specimen, i.e., the results obtained with the converged slip resistance and damage parameters given in Table 2 and Table 3. It is apparent that the Taylor factors are different for the materials due to differences in the crystallographic texture. The cast and homogenized alloys, which both have random texture, display identical Taylor factors. In contrast, the extruded alloys have different Taylor factors. The extruded AA6063 alloy has a lower Taylor factor than the cast and homogenized alloys, whereas the extruded AA6110 has a higher Taylor factor. As the crystallographic texture of the alloys evolves, the Taylor factor changes accordingly. Note that for the visco-plastic material parameters used, see Table 1, the crystal plasticity model is approximately rate insensitive so that the calculated Taylor factors are similar to the rate-independent Taylor factors (Zhang et al., 2019).

The calibration of the damage evolution and failure parameters is done by trial and error simultaneously as the slip resistance parameters are optimized. The initial damage ω_0 of each material is taken equal to the area fraction of constituent primary particles, see Section 2. The other damage parameters are fitted to the response curves from the tests on the smooth tensile specimen and the notched tensile specimen having an initial notch radius of 2 mm (R2). Table 3 contains the calibrated damage evolution and failure parameters for the different materials. Fracture is modelled by element erosion and an element is deleted when $\omega = \omega_c$ in one of the element's integration points.

5. Results

The true stress versus logarithmic strain curves from the crystal plasticity finite element simulations and the experimental tests of the smooth and notched tensile specimens are shown in Fig. 6. A good agreement is in general found between the numerical and experimental results up to fracture for both the smooth and notched specimens. This conclusion also holds for the simulations of the notched specimen with a notch radius of 0.8 mm (R0.8) which was not used in the calibration process. Prior to fracture, significant damage induced softening is observed in both the experiments and the simulations. A sharper notch radius is seen to elevate the true stress level, which is caused by the introduced triaxial stress field in the notched region. The notch radius influences the point of failure but in a different way for the different materials. For instance, for the cast and homogenized AA6063 alloy, the failure strain is significantly larger for the notched R0.8 specimen than for the notched R2 specimen, while for the extruded AA6063 alloy it is the opposite. For the extruded AA6063 alloy, the stress level for the two notched specimens is seen to overestimate the experimental results, which can be caused by several factors, as will be discussed in Section 6.

Fig. 7 presents contour plots of the von Mises equivalent plastic strain, stress triaxiality and damage in the centre of the smooth

Table 2
Crystal plasticity parameters governing initial slip resistance and work-hardening.

Material	τ_0 (MPa)	θ_1 (MPa)	τ_1 (MPa)	θ_2 (MPa)	τ_2 (MPa)
AA6063 (Cast & H.)	88.1	81.0	10.2	0.8	$8.8 \cdot 10^3$
AA6110 (Cast & H.)	116.5	86.3	14.0	0.0	0.0
AA6063 (Extruded)	84.7	200.2	20.4	0.0	0.0
AA6110 (Extruded)	96.9	177.4	21.3	3.2	$3.5 \cdot 10^6$

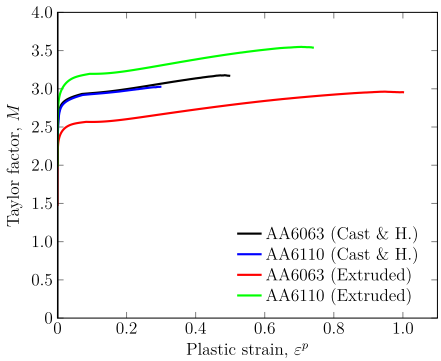

Fig. 5. Taylor factor versus plastic strain curves based on the final finite element analyses of the smooth tensile specimen for the different materials. The tensile axis is along the transverse direction (TD) for the extruded alloys.

Table 3
Crystal plasticity parameters governing damage evolution and failure.

Material	ω_0	ω_c	q_1	q_2
AA6063 (Cast & H.)	0.006	0.12	1.500	1.00
AA6110 (Cast & H.)	0.008	0.11	1.125	1.33
AA6063 (Extruded)	0.006	0.12	0.640	1.00
AA6110 (Extruded)	0.008	0.12	0.667	1.10

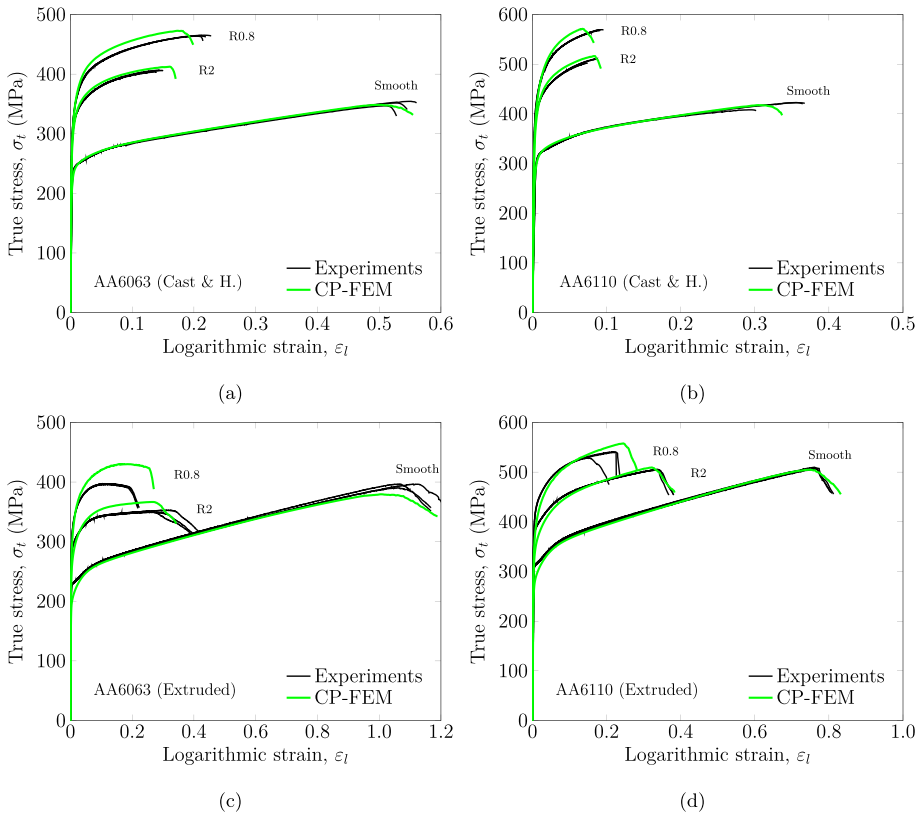

Fig. 6. True stress versus logarithmic strain curves from the experiments and corresponding finite element analyses of the smooth and notched tensile specimens: cast and homogenized (a) AA6063 alloy and (b) AA6110 alloy, and extruded (c) AA6063 alloy and (d) AA6110 alloy. The tensile axis is along the transverse direction (TD) for the extruded alloys.

tensile specimen for the extruded AA6063 alloy at a logarithmic strain of approximately $\epsilon_l \approx 0.36$. To this end, the von Mises equivalent plastic strain is defined as

$$\epsilon^p_{eq} = \int_0^t \sqrt{\frac{2}{3}\widehat{D}^p_{ij}\widehat{D}^p_{ij}}dt \tag{24}$$

Due to the distribution of crystallographic orientations between grains in the specimen, the field maps are heterogeneous. In Fig. 7a, tendencies of shear bands can be observed in the von Mises equivalent plastic strain field. These shear bands form early in the deformation process, i.e., before necking, and persist until fracture. The stress triaxiality field shown in Fig. 7b has also some band-like tendencies, but appears to be more heterogeneous than that of the plastic strain field. As a result of the heterogeneous plastic strain and stress triaxiality fields, the damage field in Fig. 7c is also heterogeneous. Initially the damage field is uniform and equal to ω_0.

The same field quantities are presented in Fig. 8 for the notched R2 specimen of the extruded AA6063 alloy at a logarithmic strain of approximately $\epsilon_l \approx 0.25$. For the notched specimens, the deformation zone is, as expected, smaller and more concentrated in the notch centre than for the smooth tensile specimen. Due to the notch geometry, the stress triaxiality is greater in magnitude and also more concentrated in the centre of the notch. The result is that the damage process zone is smaller for the notched specimens, with a higher value of the damage parameter than for the smooth specimen with the same maximum value of the von Mises equivalent plastic strain. The faster growth of the damage parameter leads to a lower logarithmic failure strain for the notched specimens. Similar trends can also be observed for the other materials.

The fracture surfaces from the crystal plasticity finite element analyses of the axisymmetric smooth and notched specimens of the cast and homogenized alloys are presented in Fig. 9. Note that we define the term fracture surface of the finite element analyses as the surface created by element erosion, which will not contain any dimples as in the experimental fracture surfaces. Due to the random texture of the cast and homogenized materials, resulting in macroscopic isotropic material properties, the deformed cross-sections remain circular, in agreement with the experimental results. Albeit the macroscopic deformation is isotropic, locally the deformation is quite heterogeneous due to differences in the crystallographic orientation between grains, creating shear bands which can be observed as contours on the exterior specimen surface next to the fracture surfaces. This local difference in both deformation and rotation of the grains contributes in developing a surface roughness, i.e., orange peel, on the exterior surfaces of the specimens. This orange peel can also to some extent be seen on the edge of the specimens in Figs. 7 and 8. Looking more thoroughly at the fracture surfaces in Fig. 9, one can see that the surfaces are not entirely flat, but resemble cup-and-cone fracture surfaces with features such as grooves and indents typically observed on experimental fracture surfaces of aluminium alloys. Fracture generally initiates somewhere in the centre of the specimens, where the stress triaxiality consistently is larger than towards the edge of the fracture surface. This

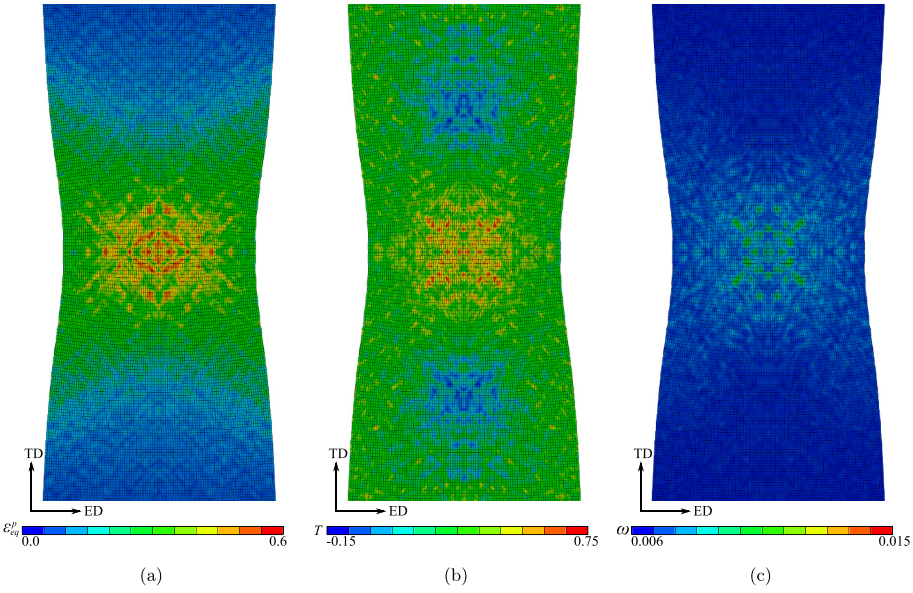

Fig. 7. Contour plots of the (a) von Mises equivalent plastic strain, (b) stress triaxiality, and (c) damage in the centre of the smooth tensile specimen for the extruded AA6063 alloy at a logarithmic strain of approximately $\epsilon_l \approx 0.36$.

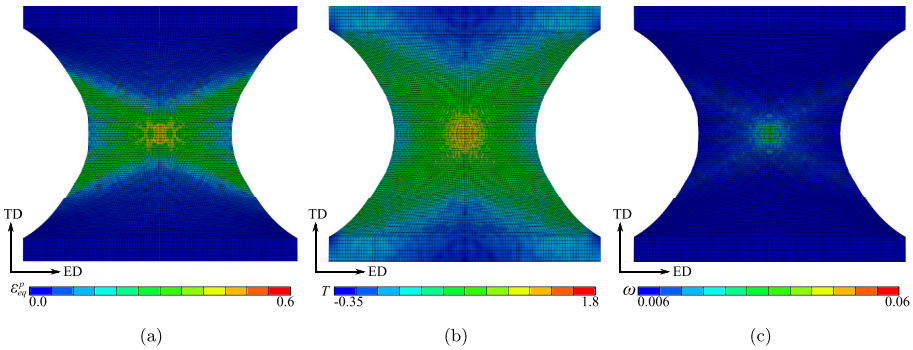

Fig. 8. Contour plots of the (a) von Mises equivalent plastic strain, (b) stress triaxiality, and (c) damage in the centre of the notched R2 tensile specimen for the extruded AA6063 alloy at a logarithmic strain of approximately $\epsilon_l \approx 0.25$.

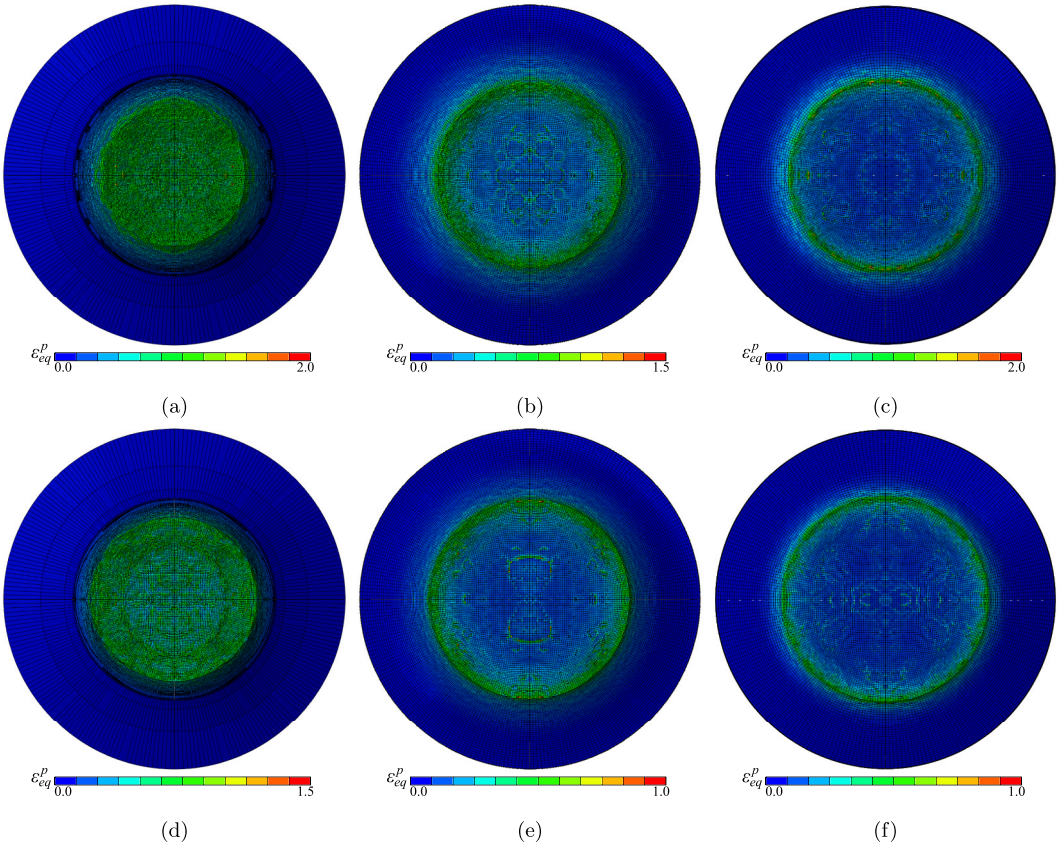

Fig. 9. Fracture surfaces of the cast and homogenized alloys in different tensile specimens predicted by the crystal plasticity finite element analyses with contours of the von Mises equivalent plastic strain. Cast and homogenized AA6063 alloy (top), and AA6110 alloy (bottom), for the smooth (left), notched R2 (middle), and notched R0.8 (right) specimens.

fracture mode results in higher levels of the von Mises equivalent plastic strain towards the edge of the final fracture surfaces, where the elements continue to deform when the elements in the centre start to erode.

Fig. 10 displays the fracture surfaces predicted by the crystal plasticity simulations of the axisymmetric smooth and notched specimens of the extruded alloys. Due to the strong crystallographic texture of the two extruded aluminium alloys, distinct shapes of the fracture surfaces are observed for the different specimens and alloys where each specimen has unique features. For the extruded AA6063 alloy, the smooth specimen exhibits a fracture surface that is somewhere between an ellipse and a rectangle in shape. In contrast, the notched specimens of the AA6063 alloy demonstrate diamond-shaped fracture surfaces, with a sharper diamond shape observed for the specimen with the sharpest notch radius. For the extruded AA6110 alloy, the smooth specimen exhibits a weakly elliptical fracture surface, while the notched specimens for this alloy display an almost circular fracture surface. Similarly to the specimens of the cast and homogenized alloys, the extruded alloys also exhibit surface roughening on the exterior of the specimens and shear bands visible as contours on the specimen surface. In general, fracture initiation occurs in the centre of the specimens, but unlike the cast and homogenized alloys, the extruded alloys typically exhibit cup-and-cup fracture surfaces.

Images of the fracture surfaces of the different specimens tested for the extruded alloys were obtained using a scanning electron microscope (SEM) and are displayed in Fig. 11. Comparing the experimental fracture surfaces with the ones predicted by the crystal plasticity finite element analyses in Fig. 10, it is apparent that the agreement is remarkable. For the smooth specimen of the extruded AA6063 alloy in Fig. 11, the upper half of the fracture surface is quite rectangular, while the bottom half is more elliptical. The simulation is not able to recreate this asymmetric feature probably caused by small local differences in material properties since only one-eighth of the specimen is modelled, but the overall shape is still predicted with reasonable accuracy. For the notched specimens of the extruded AA6063 alloy, the crystal plasticity analyses are able to predict the change in shape with a sharper notch radius observed in the experimental tests, i.e., that the diamond-shape becomes sharper with decreasing notch radius. For the extruded AA6110, the elliptical and more circular fracture surface shapes predicted by the finite element simulations agree well with the experimental

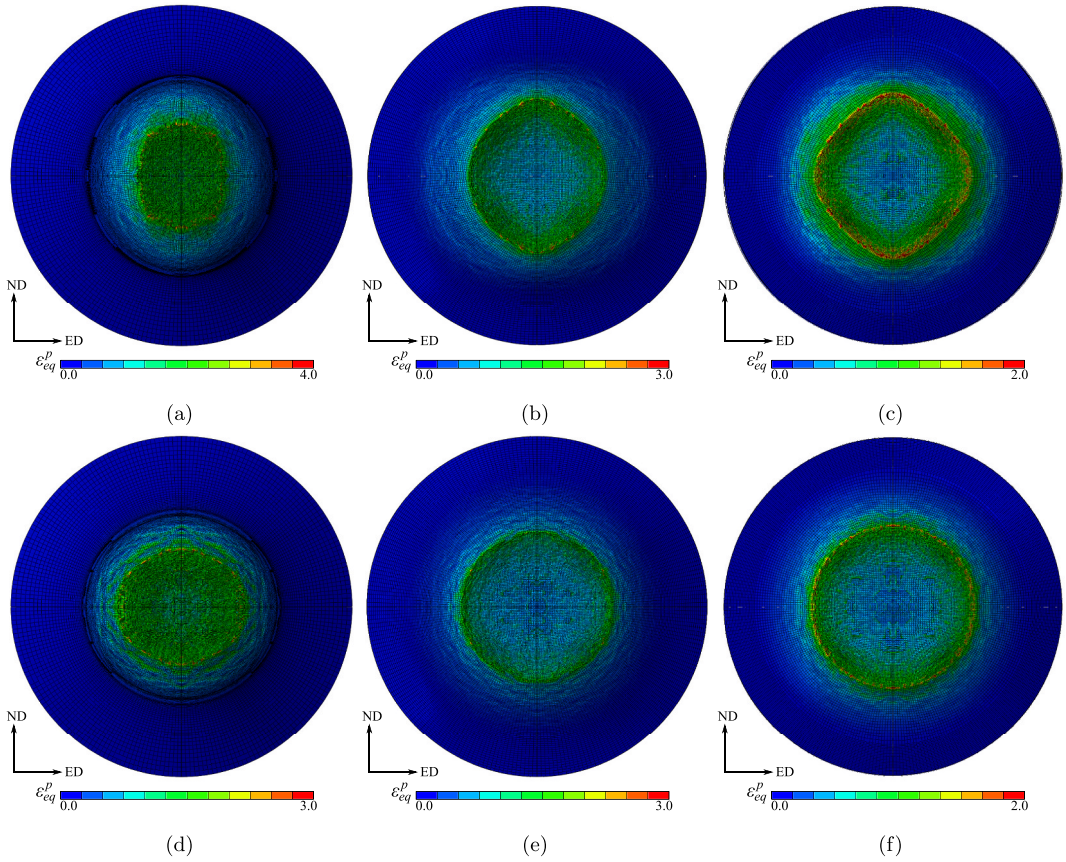

Fig. 10. Fracture surfaces of the extruded alloys in different tensile specimens predicted by the crystal plasticity finite element analyses with contours of the von Mises equivalent plastic strain. Extruded AA6063 alloy (top), and AA6110 alloy (bottom), for the smooth (left), notched R2 (middle), and notched R0.8 (right) specimens.

results.

Table 4 presents the experimental and simulated diameters of the fracture surfaces obtained for the different materials and specimen geometries, as depicted in Figs. 9–11. The good quantitative agreement between experimental and predicted diameters should be noted.

An orthographic view of the fracture surfaces of the different specimens and alloys is depicted in Figs. 12 and 13 from the crystal plasticity finite element analyses and in Fig. 14 from the experiments of the extruded AA6063 alloy. The resemblance between the numerical and experimental results is striking. On the exterior surface of both the deformed finite element models and the experimental test specimens, the orange peel is clearly visible. A cup-and-cup shaped fracture surface is observed in the finite element simulations of the extruded AA6063 alloy, resembling the cup-and-cup shape seen in the experiments. The specimens are highly deformed close to the fracture surfaces and the texture may significantly evolve in these areas, influencing the deformation of the specimen and the shape of the fracture surface.

The crystal plasticity finite element analyses were run on a workstation computer utilizing 24 threads/cores per simulation of an Intel Xeon Gold 6252 processor and the computational times are presented in Table 5. The limiting factor concerning the computational time is the time step of the explicit finite element simulations due to the small elements used. The computational time of the analyses is longer for the extruded alloys than for the cast and homogenized alloys due to the differences in ductility and element size.

6. Discussion

As mentioned in Section 5, the true stress versus logarithmic strain curves from the crystal plasticity finite element analyses of the extruded AA6063 alloy shown in Fig. 6 are seen to overestimate the experimental response for the two notched specimens. There are several possible reasons for this discrepancy. The main reason is probably that the anisotropic work-hardening behaviour and plastic flow of this alloy has previously been found to significantly depend on the heat treatment in addition to the crystallographic texture (Khadyko et al., 2017), a feature that the work-hardening model used in the present study is unable to describe. This shortcoming might influence the stress state in the notched specimens and lead to the deviations observed for this alloy.

The stress level appears to be marginally higher in the numerical simulations than in the experiments also for the notched specimens of the other materials in Fig. 6. Here, other factors can contribute such as the strength differential effect observed for aluminium alloys (Holmen et al., 2017), which is not accounted for in the proposed coupled damage and single crystal plasticity model. In addition, previously proposed single crystal porous plasticity models in the literature derived using other micromechanical homogenization principles (e.g, Han et al., 2013; Paux et al., 2015, 2018; Mbiakop et al., 2015a,b; Ling et al., 2016) typically have effective resolved shear stresses that depend on the hydrostatic stress. In the current model, this is not the case due to the properties of the Schmid's tensor and the way the effective resolved shear stresses are defined, see Equation (12). This simplification is acceptable for

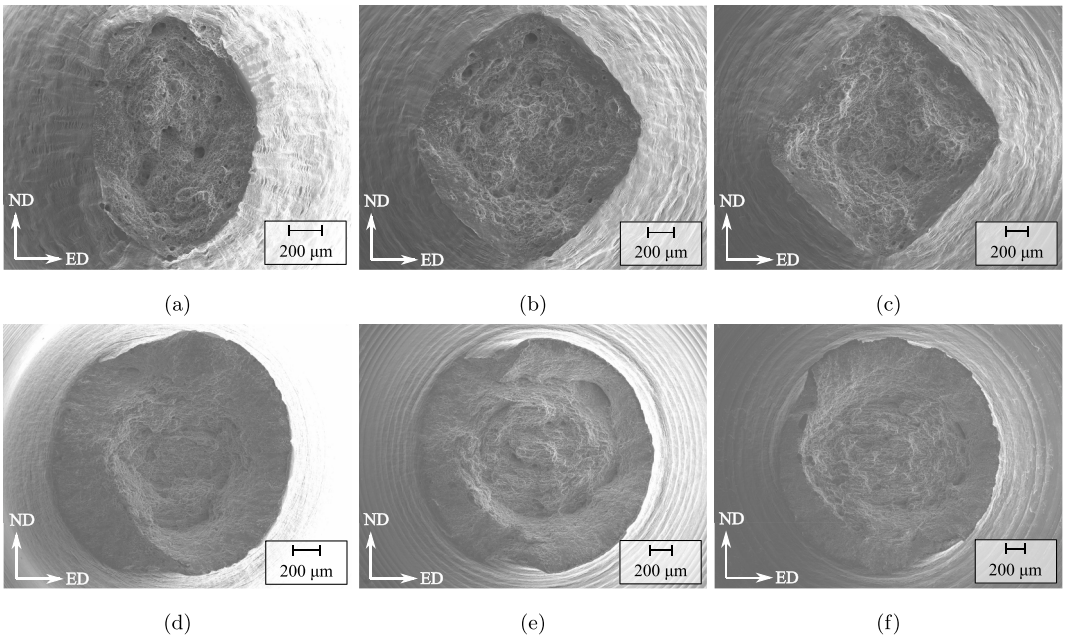

Fig. 11. Fracture surfaces of the extruded alloys in different specimens from the experimental tests of Thomesen (2019) and Thomesen et al. (2021). Extruded AA6063 alloy (top), AA6110 alloy (bottom), for the smooth (left), notched R2 (middle), and notched R0.8 (right) specimens.

Table 4
Predicted versus experimental diameters of the fracture surfaces along two perpendicular directions for the smooth and notched specimens. For the extruded materials, the diameters D_1 and D_3 are along the ED and ND, respectively.

Material	Smooth		Notch R2		Notch R0.8	
	D_1 (mm)	D_3 (mm)	D_1 (mm)	D_3 (mm)	D_1 (mm)	D_3 (mm)
AA6063 (Cast & H.)						
Experimental	4.05	4.18	4.84	4.90	5.01	5.04
Simulations	4.12	4.12	5.12	5.16	5.30	5.34
AA6110 (Cast & H.)						
Experimental	4.76	4.88	5.47	5.55	5.44	5.48
Simulations	4.80	4.84	5.52	5.56	5.68	5.74
AA6063 (Extruded)						
Experimental	1.01	1.49	1.78	1.95	2.13	2.22
Simulations	1.28	1.51	2.04	2.24	2.32	2.44
AA6110 (Extruded)						
Experimental	1.83	1.82	2.26	2.22	2.35	2.42
Simulations	1.88	1.68	2.21	2.19	2.38	2.38

Table 5
Computational time in hours for the different specimens and materials, utilizing 24 threads/cores of an Intel Xeon Gold 6252 processor.

Material	Smooth	Notch R2	Notch R0.8
AA6063 (Cast & H.)	88	151	95
AA6110 (Cast & H.)	94	84	59
AA6063 (Extruded)	396	836	350
AA6110 (Extruded)	241	491	246

reasonable values of the hydrostatic stress (see, e.g., Han et al., 2013). Due to differences in crystallographic texture, Taylor factor, strength and work hardening, the above-mentioned factors can all have a different influence on the response of the specimens depending on the material.

Although the coupled damage and single crystal plasticity model is not able to describe all the intricate details of the advanced single crystal porous plasticity models proposed in the literature, the current model is seen to predict the behaviour of different aluminium alloys with good accuracy. The proposed model is also computational efficient making it possible to simulate the behaviour of polycrystalline material test specimens or small structural components having realistic microstructures with high accuracy.

For polycrystalline materials, different neighbouring grains have different crystallographic orientations, and as a result of plastic deformation on certain crystallographic slip systems, heterogeneous stress and deformation fields develop in these materials, cf. Figs. 7 and 8. Due to these heterogeneous fields, the ductile damage process will also be heterogeneous and develop faster in certain favourable grains. In this case, the anisotropic behaviour of the single crystal making up the grain dominates the ductile fracture process as the void-induced damage grows due to plastic straining, promoting shear bands that may lead to strain localization. As a result, compatibility between differently oriented grains leads to stress concentrations that are important for strain localization, damage evolution and fracture. It thus transpires that the phenomena obtained by the discrete representation of the crystallographic texture is of utmost importance for a realistic description of ductile fracture in polycrystalline materials. The influence of the inherent heterogeneity of the polycrystal is lost in simulations using constitutive models where the plasticity and damage processes have been homogenized.

The ductile damage process depends markedly on the local stress state, and the stress triaxiality has been known for a long time to influence void growth (Pineau et al., 2016). In more recent years, the influence of the third deviatoric invariant of the stress tensor, or the Lode parameter, on ductile fracture has been addressed (e.g., Barsoum and Faleskog, 2007; 2011; Brünig et al., 2013; Dunand and Mohr, 2014). Studies have found that the Lode parameter influences the propensity for strain localization, in addition to affecting void growth and coalescence (Tekoğlu et al., 2015). The Lode parameter is thus important for ductile fracture, especially at low stress triaxiality (Pineau et al., 2016). Xue (2008) and Nahshon and Hutchinson (2008) extended the Gurson (1977) model to account for damage softening in shear by including the effect of the Lode parameter. Uncoupled damage models have also been extended to include the effect of the Lode parameter (e.g., Bai and Wierzbicki, 2010; Gruben et al., 2012; Lou et al., 2012; Mohr and Marcadet, 2015). In the model presented herein, damage evolution is amplified by the stress triaxiality ratio, while the Lode parameter has no explicit contribution to the ductile damage. Albeit the Lode parameter is not explicitly included in the expression for damage evolution, there is an implicit effect. For a polycrystalline aggregate subjected to macroscopic stress states with different Lode parameters, the local microscopic stress states and plastic flow directions will be different due to the distribution of grain orientations. These differences will affect the developing shear bands and the subsequent strain localization predicted by the coupled damage and crystal plasticity model. To disclose the importance of this implicit influence of the Lode parameter on ductile fracture, further investigations are required. A shear modification, similar to that of Xue (2008) and Nahshon and Hutchinson (2008), could readily be included in the present model, but will require additional experiments for calibration and is thus deemed outside the scope of the current work.

It is evident that the plastic anisotropy of the materials is precisely captured by the coupled damage and single crystal plasticity model, see Figs. 9–14 and Table 4. Plastic anisotropy stems primarily from the crystallographic texture of the materials (Engler and Randle, 2009), and governs the shape and evolution of the cross-section area of the different specimens during deformation. Ductile damage and fracture is also important for the final shape of the fracture surface, its topology and the formation of new free surfaces in the specimens. In addition, the coupled damage model induces material softening and accounts for the reduction of a material point's load-carrying capacity at large strains as the damage increases towards final rupture.

The finite element mesh used in the numerical simulations of the smooth and notched tensile specimens consisted of elements with a characteristic size consistent with the grain size of the different materials, except for the extruded AA6110 alloy where $30 \times 30 \times 30$ μm^3 elements were used. For this material and specimen dimensions, the fibrous grain structure with thin elongated grains and even smaller subgrains is impossible to simulate with sufficient resolution using state-of-the-art computing resources. As a consequence, the effect of crystallograpic texture and texture evolution on ductile fracture is of primary interest for this extruded alloy in the present study. For the other materials, using a higher resolution mesh with several elements per grain could have resolved the inter-grain gradients and given a more accurate description of the underlying microstructure, but at the cost of significantly increasing the computational time. Preliminary crystal plasticity finite element analyses with plane strain and axisymmetric elements indicate that the characteristic width of the shear bands is controlled by the grain size. However, with a finer discretization, i.e., several elements per grain, the enhanced resolution of the shear bands enables describing stress and strain gradients inside the grains more accurately. Also, with multiple elements inside each grain, the overall stress level becomes slightly lower.

One of the advantages of the crystal plasticity theory is its intrinsic ability to predict the change of plastic anisotropy by evolving the crystallographic texture and rotating the grains (Kalidindi et al., 2009; Ghorbanpour et al., 2020; Han et al., 2020). Thus, during plastic deformation, the crystallographic texture in the deformed area of the specimens will evolve and affect the plastic anisotropy of the highly deformed area close to the fracture surface. The evolution of the texture will influence the stress state and the plastic deformation, which in the end will affect the shape of the fracture surface. In addition to affecting the local stress state inside the material, texture evolution can also play a crucial role in the ductile fracture process by promoting or postponing strain localization. Critical grains may rotate due to plastic deformation so that, e.g., the stress state changes from a state where the void growth rate is high to a state where the void growth rate is low or vice versa, thus affecting ductile damage evolution and fracture.

Certain texture evolution phenomena can also be included in phenomenological anisotropic plasticity models to describe particular material properties. Recently, Cazacu et al. (2020) were able to predict the diamond-shaped cross-section of notched tensile specimens for a textured aluminium alloy using an anisotropic plasticity model by implicitly accounting for the effect of texture evolution. Also explicit methods of including the effects of texture evolution exist for ordinary plasticity models, e.g., the introduction of a constitutive law with plastic spin calibrated from crystal plasticity analyses (Kohar et al., 2019). Phenomenological plasticity models are often

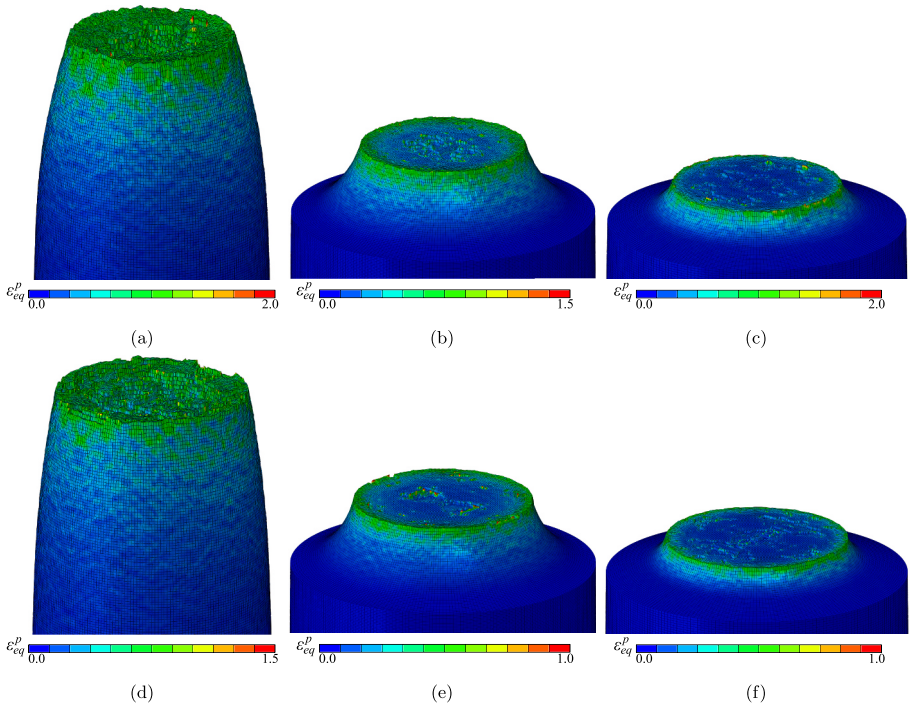

Fig. 12. Orthographic view of the fracture surfaces of the cast and homogenized alloys in different tensile specimens predicted by the crystal plasticity finite element analyses with contours of the von Mises equivalent plastic strain. Cast and homogenized AA6063 alloy (top), and AA6110 alloy (bottom), for the smooth (left), notched R2 (middle), and notched R0.8 (right) specimens.

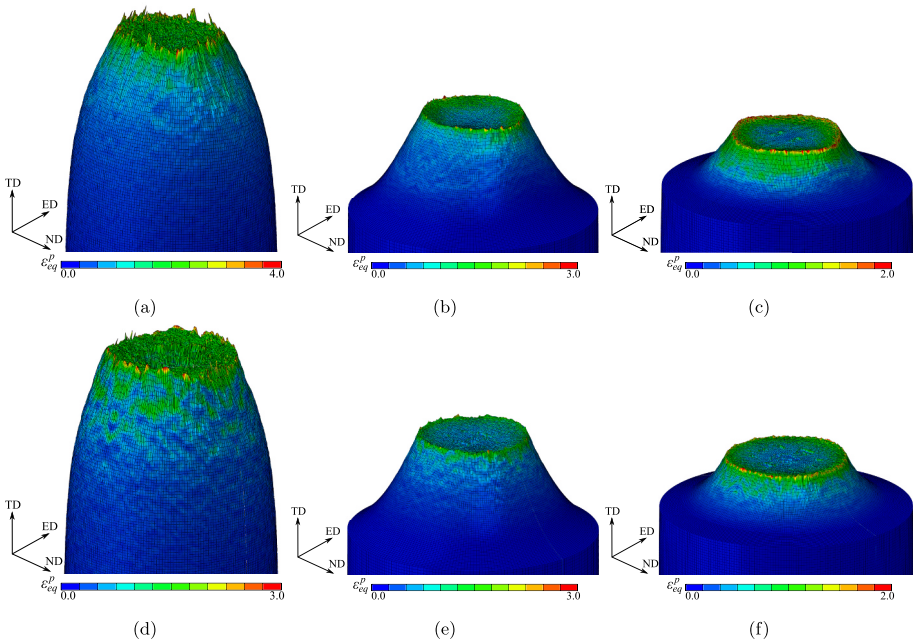

Fig. 13. Orthographic view of the fracture surfaces of the extruded alloys in different tensile specimens predicted by the crystal plasticity finite element analyses with contours of the von Mises equivalent plastic strain. Extruded AA6063 alloy (top), and AA6110 alloy (bottom), for the smooth (left), notched R2 (middle), and notched R0.8 (right) specimens.

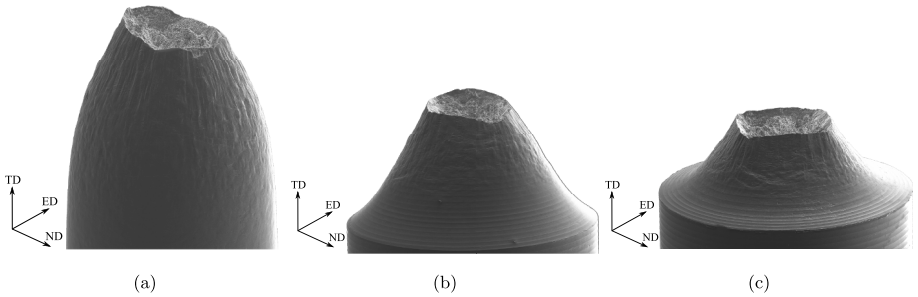

Fig. 14. Orthographic view of the fracture surfaces of the extruded AA6063 alloy in different tensile specimens from the experimental test, for the (a) smooth, (b) notched R2, and (c) notched R0.8 specimens.

preferred in finite element modelling because they are typically less computational demanding than crystal plasticity models. In general, the crystal plasticity finite element analyses require a finer finite element mesh to be able to discretize the microstructure in a realistic way, while in practical applications, ordinary plasticity models can use a coarser finite element mesh.

7. Concluding remarks

Two aluminium alloys were investigated in the cast and homogenized condition as well as in the extruded condition, giving a total of four investigated materials with different yield strength, work hardening, grain structure, crystallographic texture and tensile ductility. Finite element simulations with the proposed coupled damage and single crystal plasticity model captured the experimental behaviour in the smooth and notched tensile specimens with high accuracy. The macroscopically isotropic material behaviour of the cast and homogenized alloys was well predicted, with circular cup-and-cone fracture surfaces and features such as grooves and indents observable also on the experimental fracture surfaces. Due to the strong crystallographic texture of the two extruded aluminium alloys,

distinct cup-and-cup fracture surfaces were observed for the different specimens and alloys, with each specimen having unique features. The crystal plasticity finite element analyses captured these unique features and were also able to accurately predict the different fracture surface shapes encountered for the smooth and notched specimens.

For both the cast and homogenized and the extruded alloys, heterogeneous deformation and stress fields were observable in the specimens due to the discrete distribution of grain orientations throughout the finite element mesh. Due to these heterogeneous fields, caused by the microstructure, the ductile damage process will also be heterogeneous and evolve faster in certain favourable grains. The anisotropic behaviour of the single crystal making up the grain dominates the ductile fracture process as the void-induced damage grows due to plastic straining, promoting shear bands that lead to strain localization. Strain localization can also be promoted or postponed due to texture evolution, affecting both the local stress state and the plastic anisotropy.

The computational efficiency of the proposed coupled damage and single crystal plasticity model is higher than conventional single crystal porous plasticity models, due to the simplicity of the proposed model. The limiting factor regarding computational time is the time step of the explicit finite element analyses, where sufficiently small elements are needed to resolve the physical microstructure of polycrystalline materials. The model's accuracy, robustness and efficiency have enabled three-dimensional crystal plasticity finite element simulations of material test specimens and small structural components for ductile polycrystalline materials with ductile fracture.

CRediT authorship contribution statement

Bjørn Håkon Frodal: Conceptualization, Methodology, Software, Validation, Formal analysis, Investigation, Data curation, Writing – original draft, Writing – review & editing, Visualization. **Susanne Thomesen:** Formal analysis, Investigation, Writing – original draft, Writing – review & editing. **Tore Børvik:** Conceptualization, Writing – original draft, Writing – review & editing, Project administration, Funding acquisition. **Odd Sture Hopperstad:** Conceptualization, Methodology, Writing – original draft, Writing – review & editing, Project administration, Funding acquisition.

Declaration of competing interest

The authors declare that they have no known competing financial interests or personal relationships that could have appeared to influence the work reported in this paper.

Acknowledgements

The authors gratefully appreciate the financial support from the Norwegian University of Science and Technology (NTNU) and the Research Council of Norway through the FRINATEK Program FractAl, Project No. 250553.

References

Abaqus, 2019. Version 2019. Dassault Systemès Simulia Corporation. Providence, Rhode Island, USA.
Bachmann, F., Hielscher, R., Schaeben, H., 2010. Texture analysis with MTEX – free and open source software toolbox. Solid State Phenom. 160, 63–68.
Bai, Y., Wierzbicki, T., 2010. Application of extended Mohr–Coulomb criterion to ductile fracture. Int. J. Fract. 161, 1–20.
Barlat, F., Aretz, H., Yoon, J.W., Karabin, M.E., Brem, J.C., Dick, R.E., 2005. Linear transfomation-based anisotropic yield functions. Int. J. Plast. 21, 1009–1039.
Barsoum, I., Faleskog, J., 2007. Rupture mechanisms in combined tension and shear-micromechanics. Int. J. Solid Struct. 44, 5481–5498.
Barsoum, I., Faleskog, J., 2011. Micromechanical analysis on the influence of the lode parameter on void growth and coalescence. Int. J. Solid Struct. 48, 925–938.
Benzerga, A.A., Besson, J., 2001. Plastic potentials for anisotropic porous solids. Eur. J. Mech. Solid. 20, 397–434.
Bron, F., Besson, J., 2004. A yield function for anisotropic materials application to aluminum alloys. Int. J. Plast. 20, 937–963.
Brünig, M., Gerke, S., Hagenbrock, V., 2013. Micro-mechanical studies on the effect of the stress triaxiality and the lode parameter on ductile damage. Int. J. Plast. 50, 49–65.
Cazacu, O., Chandola, N., Revil-Baudard, B., Frodal, B.H., Børvik, T., Hopperstad, O.S., 2020. Modeling the effect of notch geometry on the deformation of a strongly anisotropic aluminum alloy. Eur. J. Mech. Solid. 82, 104004.
Dunand, M., Mohr, D., 2014. Effect of lode parameter on plastic flow localization after proportional loading at low stress triaxialities. J. Mech. Phys. Solid. 66, 133–153.
Dæhli, L.E.B., Faleskog, J., Børvik, T., Hopperstad, O.S., 2017. Unit cell simulations and porous plasticity modelling for strongly anisotropic FCC metals. Eur. J. Mech. Solid. 65, 360–383.
Eghtesad, A., Germaschewski, K., Lebensohn, R.A., Knezevic, M., 2020. A multi-GPU implementation of a full-field crystal plasticity solver for efficient modeling of high-resolution microstructures. Comput. Phys. Commun. 254, 107231.
Engler, O., Randle, V., 2009. Introduction to Texture Analysis: Macrotexture, Microtexture, and Orientation Mapping, second ed. CRC press, Taylor & Francis Group.
Feather, W.G., Lim, H., Knezevic, M., 2021. A numerical study into element type and mesh resolution for crystal plasticity finite element modeling of explicit grain structures. Comput. Mech. 67, 33–55.
Fourmeau, M., Børvik, T., Benallal, A., Lademo, O.G., Hopperstad, O.S., 2011. On the plastic anisotropy of an aluminium alloy and its influence on constrained multiaxial flow. Int. J. Plast. 27, 2005–2025.
Frodal, B.H., Christiansen, E., Myhr, O.R., Hopperstad, O.S., 2020b. The role of quench rate on the plastic flow and fracture of three aluminium alloys with different grain structure and texture. Int. J. Eng. Sci. 150, 103257.
Frodal, B.H., Dæhli, L.E.B., Børvik, T., Hopperstad, O.S., 2019. Modelling and simulation of ductile failure in textured aluminium alloys subjected to compression-tension loading. Int. J. Plast. 118, 36–69.

Frodal, B.H., Morin, D., Børvik, T., Hopperstad, O.S., 2020a. On the effect of plastic anisotropy, strength and work hardening on the tensile ductility of aluminium alloys. Int. J. Solid Struct. 188–189, 118–132.
Ghorbanpour, S., Alam, M.E., Ferreri, N.C., Kumar, A., McWilliams, B.A., Vogel, S.C., Bicknell, J., Beyerlein, I.J., Knezevic, M., 2020. Experimental characterization and crystal plasticity modeling of anisotropy, tension-compression asymmetry, and texture evolution of additively manufactured inconel 718 at room and elevated temperatures. Int. J. Plast. 125, 63–79.
Gruben, G., Hopperstad, O.S., Børvik, T., 2012. Evaluation of uncoupled ductile fracture criteria for the dual-phase steel docol 600dl. Int. J. Mech. Sci. 62, 133–146.
Gurson, A.L., 1977. Continuum theory of ductile rupture by void nucleation and growth: Part I—yield criteria and flow rules for porous ductile media. J. Eng. Mater. Technol. 99, 2–15.
Han, F., Diehl, M., Roters, F., Raabe, D., 2020. Using spectral-based representative volume element crystal plasticity simulations to predict yield surface evolution during large scale forming simulations. J. Mater. Process. Technol. 277, 116449.
Han, X., Besson, J., Forest, S., Tanguy, B., Bugat, S., 2013. A yield function for single crystals containing voids. Int. J. Solid Struct. 50, 2115–2131.
Hill, R., 1948. A theory of the yielding and plastic flow of anisotropic metals. Proc. Roy. Soc. Lond.: Mathematical, Physical and Engineering Sciences 193, 281–297.
Holmen, J.K., Frodal, B.H., Hopperstad, O.S., Børvik, T., 2017. Strength differential effect in age hardened aluminum alloys. Int. J. Plast. 99, 144–161.
Hutchinson, J.W., 1976. Bounds and self-consistent estimates for creep of polycrystalline materials. Proc. Roy. Soc. Lond.: Mathematical, Physical and Engineering Sciences 348, 101–127.
Joëssel, L., Vincent, P.G., Garajeu, M., Idiart, M.I., 2018. Viscoplasticity of voided cubic crystals under hydrostatic loading. Int. J. Solid Struct. 147, 156–165.
Kalidindi, S.R., Donohue, B.R., Li, S., 2009. Modeling texture evolution in equal channel angular extrusion using crystal plasticity finite element models. Int. J. Plast. 25, 768–779.
Khadyko, M., Dumoulin, S., Børvik, T., Hopperstad, O.S., 2015. Simulation of large-strain behaviour of aluminium alloy under tensile loading using anisotropic plasticity models. Comput. Struct. 157, 60–75.
Khadyko, M., Dumoulin, S., Cailletaud, G., Hopperstad, O.S., 2016. Latent hardening and plastic anisotropy evolution in AA6060 aluminium alloy. Int. J. Plast. 76, 51–74.
Khadyko, M., Frodal, B.H., Hopperstad, O.S., 2021. Finite element simulation of ductile fracture in polycrystalline materials using a regularized porous crystal plasticity model. Int. J. Fract. 228, 15–31.
Khadyko, M., Marioara, C.D., Dumoulin, S., Børvik, T., Hopperstad, O.S., 2017. Effects of heat-treatment on the plastic anisotropy of extruded aluminium alloy AA6063. Mater. Sci. Eng. 708, 208–221.
Knezevic, M., Drach, B., Ardeljan, M., Beyerlein, I.J., 2014. Three dimensional predictions of grain scale plasticity and grain boundaries using crystal plasticity finite element models. Comput. Methods Appl. Mech. Eng. 277, 239–259.
Kohar, C.P., Bassani, J.L., Brahme, A., Muhammad, W., Mishra, R.K., Inal, K., 2019. A new multi-scale framework to incorporate microstructure evolution in phenomenological plasticity: theory, explicit finite element formulation, implementation and validation. Int. J. Plast. 117, 122–156.
Le Roy, G., Embury, J.D., Edwards, G., Ashby, M.F., 1981. A model of ductile fracture based on the nucleation and growth of voids. Acta Metall. 29, 1509–1522.
Lemaitre, J., 1985. A continuous damage mechanics model for ductile fracture. J. Eng. Mater. Technol. 107, 83–89.
Ling, C., Besson, J., Forest, S., Tanguy, B., Latourte, F., Bosso, E., 2016. An elastoviscoplastic model for porous single crystals at finite strains and its assessment based on unit cell simulations. Int. J. Plast. 84, 58–87.
Lou, Y., Huh, H., Lim, S., Pack, K., 2012. New ductile fracture criterion for prediction of fracture forming limit diagrams of sheet metals. Int. J. Solid Struct. 49, 3605–3615.
Maire, E., Zhou, S., Adrien, J., Dimichiel, M., 2011. Damage quantification in aluminium alloys using in situ tensile tests in x-ray tomography. Eng. Fract. Mech. 78, 2679–2690.
Mbiakop, A., Constantinescu, A., Danas, K., 2015a. A model for porous single crystals with cylindrical voids of elliptical cross-section. Int. J. Solid Struct. 64–65, 100–119.
Mbiakop, A., Constantinescu, A., Danas, K., 2015b. An analytical model for porous single crystals with ellipsoidal voids. J. Mech. Phys. Solid. 84, 436–467.
McClintock, F.A., 1968. A criterion for ductile fracture by the growth of holes. J. Appl. Mech. 35, 363–371.
Mohr, D., Marcadet, S.J., 2015. Micromechanically-motivated phenomenological Hosford–Coulomb model for predicting ductile fracture initiation at low stress triaxialities. Int. J. Solid Struct. 67–68, 40–55.
Nahshon, K., Hutchinson, J.W., 2008. Modification of the gurson model for shear failure. Eur. J. Mech. Solid. 27, 1–17.
Needleman, A., 1972. Void growth in an elastic-plastic medium. J. Appl. Mech. 39, 964–970.
Paux, J., Brenner, R., Kondo, D., 2018. Plastic yield criterion and hardening of porous single crystals. Int. J. Solid Struct. 132–133, 80–95.
Paux, J., Morin, L., Brenner, R., Kondo, D., 2015. An approximate yield criterion for porous single crystals. Eur. J. Mech. Solid. 51, 1–10.
Pineau, A., Benzerga, A.A., Pardoen, T., 2016. Failure of metals I: Brittle and ductile fracture. Acta Mater. 107, 424–483.
Rice, J.R., Tracey, D.M., 1969. On the ductile enlargement of voids in triaxial stress fields. J. Mech. Phys. Solid. 17, 201–217.
Rousselier, G., 1987. Ductile fracture models and their potential in local approach of fracture. Nucl. Eng. Des. 105, 97–111.
Rousselier, G., 2021. Porous plasticity revisited: macroscopic and multiscale modeling. Int. J. Plast. 136, 102881.
Rousselier, G., Leclercq, S., 2006. A simplified “polycrystalline” model for viscoplastic and damage finite element analyses. Int. J. Plast. 22, 685–712.
Rousselier, G., Luo, M., 2014. A fully coupled void damage and mohr–coulomb based ductile fracture model in the framework of a reduced texture methodology. Int. J. Plast. 55, 1–24.
Savage, D.J., Chandola, N., Cazacu, O., McWilliams, B.A., Knezevic, M., 2018. Validation of recent analytical dilatational models for porous polycrystals using crystal plasticity finite element models with schmid and non-schmid activation laws. Mech. Mater. 126, 148–162.
Siddiq, A., 2019. A porous crystal plasticity constitutive model for ductile deformation and failure in porous single crystals. Int. J. Damage Mech. 28, 233–248.
Song, D., Ponte Castañeda, P., 2017. A finite-strain homogenization model for viscoplastic porous single crystals: I – theory. J. Mech. Phys. Solid. 107, 560–579.
Steglich, D., Wafai, H., Besson, J., 2010. Interaction between anisotropic plastic deformation and damage evolution in Al 2198 sheet metal. Eng. Fract. Mech. 77, 3501–3518.
Tekoğlu, C., Hutchinson, J.W., Pardoen, T., 2015. On localization and void coalescence as a precursor to ductile fracture. Phil. Trans. Math. Phys. Eng. Sci. 373, 20140121.
Thomesen, S., 2019. Plastic flow and fracture of isotropic and anisotropic 6000-series aluminium alloys: experiments and numerical simulations. Ph.D. thesis. NTNU.
Thomesen, S., Hopperstad, O.S., Børvik, T., 2021. Anisotropic plasticity and fracture of three 6000-series aluminium alloys. Metals 11 (4), 557.
Thomesen, S., Hopperstad, O.S., Myhr, O.R., Børvik, T., 2020. Influence of stress state on plastic flow and ductile fracture of three 6000-series aluminium alloys. Mater. Sci. Eng. 783, 139295.
Tvergaard, V., 1981. Influence of voids on shear band instabilities under plane strain conditions. Int. J. Fract. 17, 389–407.
Weck, A., Wilkinson, D.S., Maire, E., Toda, H., 2008. Visualization by x-ray tomography of void growth and coalescence leading to fracture in model materials. Acta Mater. 56, 2919–2928.
Wu, P.D., Lloyd, D.J., Jain, M., Neale, K.W., Huang, Y., 2007. Effects of spatial grain orientation distribution and initial surface topography on sheet metal necking. Int. J. Plast. 23, 1084–1104.
Xue, L., 2008. Constitutive modeling of void shearing effect in ductile fracture of porous materials. Eng. Fract. Mech. 75, 3343–3366.
Zecevic, M., Knezevic, M., 2018. Latent hardening within the elasto-plastic self-consistent polycrystal homogenization to enable the prediction of anisotropy of AA6022-T4 sheets. Int. J. Plast. 105, 141–163.
Zhang, F., Bower, A.F., Mishra, R.K., Boyle, K.P., 2009. Numerical simulations of necking during tensile deformation of aluminum single crystals. Int. J. Plast. 25, 49–69.

Zhang, K., Geng, X., Li, J., Hu, R., 2007. On the tension necking of copper single crystal specimen under slip deformation mechanism. Sci. China E 50, 308–318.
Zhang, K., Holmedal, B., Mánik, T., Saai, A., 2019. Assessment of advanced taylor models, the taylor factor and yield-surface exponent for FCC metals. Int. J. Plast. 114, 144–160.
Zhang, K., Hopperstad, O.S., Holmedal, B., Dumoulin, S., 2014. A robust and efficient substepping scheme for the explicit numerical integration of a rate-dependent crystal plasticity model. Int. J. Numer. Methods Eng. 99, 239–262.